

Star Formation and Metallicity Gradients in Semi-analytic Models of Disk Galaxy Formation

Jian Fu¹ ^{*}, Guinevere Kauffmann¹, Mei-ling Huang¹, Robert M. Yates¹,
Sean Moran², Timothy M. Heckman³, Romeel Davé⁴, Qi Guo^{5,6}

¹*Max-Planck-Institut für Astrophysik, D-85741 Garching, Germany*

²*Harvard-Smithsonian Center for Astrophysics, 60 Garden Street, Cambridge, MA 02138, USA*

³*Department of Physics and Astronomy, The Johns Hopkins University, MD21218, Baltimore, USA*

⁴*Astronomy Department, University of Arizona, AZ85721, Tucson, USA*

⁵*National Astronomical Observatories, CAS, Beijing 100012, China*

⁶*Institute for Computational Cosmology, Department of Physics, University of Durham, South Road, Durham, DH1 3LE, UK*

2 December 2024

ABSTRACT

We have updated our radially-resolved semi-analytic models of galaxy formation to track the radial distribution of stars, metals, atomic and molecular gas in galactic disks. The models are run on dark matter halo merger trees from the Millennium and Millennium II simulations using the physical recipes outlined in Fu et al. (2010) and Guo et al. (2011), with 3 main changes: (1) We adopt a simple star formation law where the star formation rate surface density is proportional to the surface density of molecular gas ($\Sigma_{\text{SFR}} \propto \Sigma_{\text{H}_2}$). (2) We inject a fraction of the heavy elements produced by supernovae directly into the halo, instead of first mixing them with the cold gas in the disk. (3) We include radial gas inflows in disks using a model of the form $v_{\text{inflow}} = \alpha r$.

The average surface density profiles of molecular gas in L_* galaxies place strong constraints on inflow velocities, favouring models where $v_{\text{inflow}} \sim 7$ km/s at a galactocentric radius of 10 kpc. The radial inflow model has little influence on the gas and stellar metallicity gradients in the outer regions of galaxies. Gas-phase metallicity gradients are affected much more strongly by the fraction of metals that are directly injected into the halo gas, rather than mixed with the interstellar cold gas of the galaxy. Metals ejected out of the galaxy at early epochs result in late infall of pre-enriched gas and *flatter* present-day gas-phase metallicity gradients. A prescription in which 80 % of all the metals produced by stars are injected into the halo gas provides the best fit to the relatively flat observed metallicity gradients of galaxies with stellar masses greater than $10^{10} M_{\odot}$. Such a prescription also results in a good fit to the relation between gas-phase metallicity and specific star formation rate in the outer parts of galactic disks. We examine the correlation between gas-phase metallicity gradient and a number of global galaxy properties, finding that it is most strongly correlated with the bulge-to-disk ratio of the galaxy. This is because gas is consumed when the bulge forms during the galaxy merger, and the gas-phase metallicity gradient is then set by newly-accreted gas. These model predictions appear to be in good agreement with observations from Moran et al. (2012).

Key words: galaxies: evolution - galaxies: formation - stars: formation - galaxies: ISM - ISM: atoms - ISM: molecules

1 INTRODUCTION

In recent years, observations of radially resolved profiles of atomic gas, molecular gas and star formation in represen-

tative samples nearby galaxies (e.g THINGS for HI profiles, Walter et al. 2008; HERACLES for H₂ profiles, Leroy et al. 2009) have motivated galaxy formation theorists to include the physics of the atomic-to-molecular gas transition in their models. Some of these models make predictions for the global atomic and molecular gas content of

^{*} E-mail: fujian@mpa-garching.mpg.de

galaxies (e.g. Obreschkow et al. 2009; Lagos et al. 2011), while others attempt to model the radial structure of the gas in more detail (e.g. Robertson & Kravtsov 2008; Fu et al. 2010; Power, Baugh & Lacey 2010; Feldmann, Hernandez & Gnedin 2012). Radial abundance gradients also place important constraints on disk formation models, particularly on how supernova feedback (SN feedback) processes eject metals into the surrounding gas and how these metals are mixed throughout the disk as the galaxy evolves. A successful model of disk galaxy formation should be able to reproduce the metallicity gradients in galaxies along with radial density profiles of old stars, young stars and gas.

Observational data on metal abundance gradients in galaxies remains rather sparse. Many studies focus only on one galaxy or on a handful of galaxies (e.g. Rudolph et al. 2006 for the Milky Way; Magrini et al. 2007 for M33; Bresolin et al. 2009 for M83). For many years, the Zaritsky, Kennicutt & Huchra (1994) study of gas-phase metallicity gradients derived for 159 HII regions in 14 spiral galaxies in combination with published data for another 25 galaxies, has remained the standard reference in the field. More recently, Moustakas et al. (2010) published metallicity gradients for 65 galaxies from the SINGS survey and Moran et al. (2012; hereafter Moran12) analyzed gradients for 174 galaxies with atomic and molecular gas mass measurements from the GASS and COLD GASS surveys (Catinella et al. 2010; Saintonge et al. 2011a). These new observations make it possible to carry out a statistical comparison with model predictions for the first time.

There is a long history of models of the radial structure and properties of disk galaxies in the literature, beginning with Tinsley & Larson (1978) who implemented a model for chemical evolution into the dynamical collapse calculations for gas clouds with rotation and axial symmetry introduced by Larson (1976). Similar modelling efforts were later undertaken by many others (e.g. Matteucci & Franco 1989; Kauffmann 1996; Chiappini, Matteucci & Gratton 1997; Dalcanton, Spergel & Summers 1997; Avila-Reese, Firmani, & Hernández 1998; van den Bosch 1998; Prantzos 1999; Dutton et al. 2007; Fu et al. 2009; Yin et al. 2009; Cook et al. 2010; Fu et al. 2010). The models can be arranged in increasing order of complexity, from those that use simple parameterized formulae to describe the infall of gas onto the disk, to those that are embedded within high resolution N-body simulations of structure formation in a Λ CDM cosmology and where gas infall rates are determined by explicitly following the growth of each dark matter halo in the simulation and then calculating the rate at which gas will cool as a function of time.

In order to model the radial distributions of stars and gas in the disk, processes such as star formation, SN feedback and chemical enrichment need to be treated in a radially resolved fashion. In previous work (Fu et al. 2010, hereafter Fu10), we developed models in which each galaxy disk was divided into a series of concentric rings. We adopted two different prescriptions to partition the cold gas into atomic and molecular components: one is adapted from the models of Krumholz, McKee & Tumlinson (2009), in which the H_2 fraction is parameterized as a function of local cold gas surface density and gas-phase metallicity. The other prescription is empirically-based and proposes that the H_2 fraction is related to the interstellar pressure (Elmegreen 1989 & 1993;

Blitz & Rosolowsky 2004 & 2006). The Fu10 semi-analytic model is based on the version of the L-Galaxies code described in De Lucia & Blaizot (2007) (hereafter DLB07) implemented on the halo merger trees of the Millennium Simulation outputs (Springel et al. 2005). As discussed in the paper, the model reproduces the radial profiles of stellar mass, HI, H_2 , and star formation in L_* galaxies. However, the model produces a stellar mass function that is too steep at the faint end and the gas fractions of low mass galaxies do not agree with observations.

The analysis presented in this paper is based on the new version of the L-Galaxies code described in Guo et al. (2011) (hereafter Guo11), which runs on the halo merger trees of both the Millennium Simulation (Springel et al. 2005) and on the 125 times higher resolution Millennium II Simulation (Boylan-Kolchin et al. 2009). This allows us to study the formation and evolution of galaxies with masses ranging from those of dwarfs to the most massive cD galaxies.

Our paper is organized as follows. In Section 2, we briefly describe the N-body simulation, and the changes to the semi-analytic model with respect to Fu10 and Guo11. We discuss how we normalize the free parameters in our models using gas profile data from Leroy et al. (2008) for a small sample of nearby disks, along with the stellar and gas mass functions of nearby galaxies at $z = 0$. In Section 3, we present stellar, HI and H_2 mass functions at $z = 0$ and compare them to observations. In Section 4, we analyze how the star formation rate surface density profiles of galaxies depend on stellar mass. In Section 5, we study how the radial profiles of gas-phase metallicity depend on stellar mass, bulge-to-disk ratio, stellar surface density and specific star formation rate. We also look at the relations between metallicity and star formation in the inner and outer disks of galaxies. The model results presented in Sections 4 and 5 are compared to observational results from Moran12. Finally, in Section 6, we summarize our results and discuss avenues for future work.

2 THE MODELS

2.1 The N-body simulations

The galaxy formation models are run on two very large N-Body simulations: the Millennium Simulation (hereafter MS, Springel et al. 2005) and Millennium-II Simulation (hereafter MS-II, Boylan-Kolchin et al. 2009). Both simulations adopt a Λ CDM cosmogony with parameters $\Omega_\Lambda = 0.75$, $\Omega_m = 0.25$, $\Omega_{\text{baryon}} = 0.045$, $\sigma_8 = 0.9$ and $h = 0.73$, and they track $2160^3 \approx 10^{10}$ particles from $z = 127$ to $z = 0$. The main difference between the two simulations is the resolution. The particle mass in MS is $8.6 \times 10^8 M_\odot h^{-1}$ and the periodic box is $500 \text{ Mpc } h^{-1}$ on a side; the particle mass in MS-II is $6.8 \times 10^6 M_\odot h^{-1}$ and the size of the periodic box is $100 \text{ Mpc } h^{-1}$, which means the resolution of MS-II is 125 times higher than MS. Since the smallest halo traced in both simulations has 20 particles, MS can be used to study the formation and evolution for Milky Way-sized or larger galaxies, while MS-II is more appropriate to study dwarf galaxies. For our models of the cold gas components in galaxies, the MS is suitable to study atomic and molecular gas for disk galaxies with stellar mass $M_* \gtrsim 10^{10} M_\odot$ and MS-II

is useful to study the gas components in present-day dwarf galaxies and in the high-redshift progenitors of present-day L_* galaxies. Another difference between the two simulations is the number of output snapshots: the last 60 snapshots for MS and MS-II are identical, but MS-II has more snapshots at very high redshift to increase the time resolution in early-forming first structures.

2.2 The galaxy formation models

The reader is referred to Section 3 of Guo11 for a detailed discussion of how the various physical processes in the model are calculated, including re-ionization, gas infall and cooling, star formation and metal production, SN feedback, ram-pressure stripping of gas in satellite galaxies, tidal disruption of satellites, galaxy mergers, bulge formation, black hole growth and AGN feedback.

The cosmological parameters for both MS and MS-II and the semi-analytic models in DLB07 and Guo11 are from WMAP1 (Wilkinson Microwave Anisotropy Probe) first-year results (Spergel et al. 2003). To update the cosmology, Guo et al. (2013, hereafter Guo13) adopt the technique described in Angulo & White (2010) to rescale the growth of structure to be appropriate for WMAP7 parameters ($\Omega_\Lambda = 0.728$, $\Omega_m = 0.272$, $\Omega_{\text{baryon}} = 0.0454$, $\sigma_8 = 0.807$ and $h = 0.704$; Komatsu et al. 2011). We make use of these rescaled models in this paper, but we note that differences for the quantities explored in this paper are negligible compared to systematic uncertainties in our treatment of the various gas-physical processes.

The main changes made in this paper with respect to Guo11 are the following: (1) We include the methodology to track gas and stellar components in radial rings described in Fu10. (2) We include the prescriptions for the transition between atomic gas and molecular gas described in Fu10. (3) We abandon the two-regime star formation model in Fu10 and adopt a simpler prescription where the star formation surface density is always proportional to the molecular gas surface density (e.g. Leroy et al. 2008; Bigiel et al. 2008; Schruba et al. 2011). (4) We allow a fraction of heavy elements to be mixed directly with the hot gas in the halo. We describe these modifications in more detail below.

2.3 Treatment of the radial distribution of gas in disks

In this paper, we divide each disk into 12 rings instead of 30 rings as in Fu10. This is done to decrease the computational memory requirements. The ring radii are given by the geometric series

$$r_i = 0.44 \times 1.5^i [h^{-1} \text{kpc}] \quad (i = 1, 2, \dots, 12) \quad (1)$$

The radius for the innermost ring in Eq. (1) is about 0.9 kpc, and the radius for the outermost ring is about 80 kpc. As we mentioned in Fu10, the radial profiles are insensitive to the precise scheme, if the adopted number of rings is sufficiently large. This sub-division of the disk in Eq. (1) is sufficient to study both small and large galaxies.

2.3.1 The radial distribution of gas cooling onto the galaxy disks

We adopt the same prescription described in Fu10, in which newly infalling cold gas at each time step has exponential form with scale length $r_{\text{infall}} = r_d = (\lambda/\sqrt{2}) r_{\text{vir}}$ (Mo, Mao & White 1998). Gas is simply added to each radial ring such that it follows this profile.

2.3.2 Mergers, bulge formation and the radial distribution of bulge stars

The DLB07 model does not include a prescription for bulge sizes and the Fu10 model did not attempt to calculate the radial distribution of bulge stars. The Guo11 models include a method for calculating the sizes of bulges produced during galaxy mergers and by disc instabilities.

The size of the bulge after a merger is calculated using the following equation

$$C \frac{m_{\text{new}}^2}{r_{\text{new}}} = C \frac{m_1^2}{r_1} + C \frac{m_2^2}{r_2} + \alpha \frac{m_1 m_2}{r_1 + r_2} \quad (2)$$

where C parametrizes the binding energy of the galaxy and α parametrizes the effective interaction energy deposited in the stellar components. In Guo11, $C = 0.5$ and $\alpha = 0.5$ are adopted for galaxy mergers. m_{new} and r_{new} in Eq. (2) are the mass and half mass radius of the newly formed bulge. For major mergers, in which the ratio of the total (stellar+gas) mass of the satellite to the central galaxy is larger than 0.3, both disks are destroyed. The stars in both progenitor galaxies and the stars formed in the merger-induced starburst become bulge stars. In this case, m_1 is sum of the stellar mass of the two progenitor galaxies and m_2 is the sum of the stellar mass converted from cold gas in the major merger starburst (see later); r_1 and r_2 are the corresponding half-mass radii.

For a minor merger ($m_{\text{sat}}/m_{\text{cen}} < 0.3$), the stellar component of the smaller satellite galaxy is added to the bulge of the central galaxy, while the cold gas component of the satellite is added to the disk of the central galaxy. m_1 in Eq. (2) is the bulge mass of the central galaxy before the merger and m_2 is the stellar mass (bulge+disk) of the satellite galaxy; r_1 and r_2 are the corresponding half mass radii.

The main new prescription implemented in this paper concerns the radial profile of gas added to the central galaxy from the satellite before the starburst occurs. The Fu10 code directly superposes the gas radial profiles of two gas disks together and then processes the starburst. In this paper, we treat the accreted gas from the satellite in the same way as gas cooling from the halo; the scale length of the accreted gas is determined from the spin parameter and virial radius of the halo of the central galaxy using the equation $r_{\text{infall}} = (\lambda/\sqrt{2}) r_{\text{vir}}$.

The DLB07 and Guo11 codes use the ‘‘collisional starburst model’’ introduced by Somerville, Primack & Faber (2001). In both major and minor mergers, the mass of stars formed in the starburst is $m_* = e_{\text{burst}} m_{\text{gas}}$, with e_{burst} given by the equation

$$e_{\text{burst}} = \beta_{\text{burst}} (m_{\text{sat}}/m_{\text{cen}})^{\alpha_{\text{burst}}} \quad (3)$$

with $\alpha_{\text{burst}} = 0.7$ and $\beta_{\text{burst}} = 0.56$.

In our model, we simply calculate the surface mass density of stars formed in the burst in ring number i as

$$\Sigma_{*,i} = e_{\text{burst}} \Sigma_{\text{gas},i} \quad (4)$$

using Eq. (3) to define e_{burst} . For starbursts occurring during major mergers, the stars formed in all the rings become bulge stars.

This is admittedly not a very realistic description of what happens in an actual merger-induced starburst, but since we mainly study quiescent disk galaxies in this paper, this will not concern us. The other update we make with respect to the Guo11 models during mergers is to calculate the half mass radii directly from the stellar and gas profiles, rather than to assume an exponential form.

Bulges also form through secular evolution. When $v_{\text{max}} < \sqrt{G m_{*,\text{disk}} / r_{*,\text{disk}}}$, the disk is considered unstable. A mass δm_* from the inner part of the disk is transferred to the bulge

$$\delta m_* = m_{*,\text{disk}} - \frac{r_{*,\text{disk}} v_{\text{max}}^2}{G} \quad (5)$$

where $m_{*,\text{disk}}$ and $r_{*,\text{disk}}$ are the mass and scale length of the stellar disk. If this material forms a new bulge, it is assumed to have a half-mass radius δr equal to the outer radius of the region. If there is already a bulge in the galaxy, then the resulting bulge is calculated using

$$0.5 \frac{m_{\text{new}}^2}{r_{\text{new}}} = 0.5 \frac{m_1^2}{r_1} + 0.5 \frac{m_2^2}{r_2} + 2.0 \frac{m_1 m_2}{r_1 + r_2} \quad (6)$$

where m_1 and r_1 are the mass and half mass radius of the existing bulge; $m_2 = \delta m_*$ and $r_2 = \delta r$ are the mass and radius of the transferred region. Once again we have updated this prescription by calculating the radius δr directly from the stellar radial distribution of the disk rather than by assuming an exponential stellar disk profile as in Guo11.

As in Guo11, we assume a Jaffe profile (Jaffe 1983) for the bulge of the form

$$\rho_{\text{bulge}}(r) = \frac{m_{\text{bulge}}}{4\pi r_b^3} \left(\frac{r}{r_b} \right)^{-2} \left(1 + \frac{r}{r_b} \right)^{-2} \quad (7)$$

in which m_{bulge} is the bulge mass and r_b is the half mass radius of the galaxy bulge. The stellar mass in a given radial ring is the combined mass of disk and bulge stars in that ring:

$$\begin{aligned} m_* &= m_{*,\text{disk}} + 4\pi \int_{r_{\text{in}}}^{r_{\text{out}}} \rho_{\text{bulge}}(r) r^2 dr \\ &= m_{*,\text{disk}} + m_{\text{bulge}} \left[\left(1 + \frac{r_{\text{in}}}{r_b} \right)^{-1} - \left(1 + \frac{r_{\text{out}}}{r_b} \right)^{-1} \right] \end{aligned} \quad (8)$$

where $m_{*,\text{disk}}$ is the stellar mass of the disk component in the ring, and r_{in} , r_{out} are the inner and outer radii of the radial ring. We note that the stellar surface density profiles presented in the next sections include both bulge and disk components.

2.3.3 Radial gas inflows in disks

In Fu10, we showed that a star formation law of form $\Sigma_{\text{SFR}} \propto \Sigma_{\text{H}_2}$ was problematic in that it led to cold gas surface density profiles that were too shallow to match observations (see Sec. 3.4 & Fig. 3 in Fu10). In that paper, we

introduced the following two tweaks to solve the problem: (i) we adopted a star formation law in regions of the disk with $f_{\text{H}_2} < 0.5$ of the form $\Sigma_{\text{SFR}} \propto \Sigma_{\text{gas}}^2$. (ii) we assumed that the SN reheating efficiency was inversely proportional to gas surface density ($\Delta m_{\text{reheat}} \propto \Delta m_*/\Sigma_{\text{gas}}$). The second assumption increases the gas consumption timescale in the inner disk.

In this paper, we will introduce a radial gas inflow prescription as a more realistic solution, i.e the gas from the outer disk flows inwards towards the inner disk. As we will now show, a plausible inflow prescription combined with a simpler star formation law in which the star formation rate surface density is always proportional to the molecular gas surface density, produces gas surface density profiles that match observations without need for a radially-dependent SN feedback efficiency.

There are a number of physical mechanisms that can drive radial inflows of gas in the disk. The ones that are invoked most frequently involve gravitational interaction between gas in the disk and non-axisymmetric stellar structures such as bars and spiral structures (Kalnajs 1972). Simple physical considerations yield estimates of flow velocities ranging from 0.1 to a few km/s (Lacey & Fall 1985; Bertin & Lin 1996). Attempts to measure radial flow rates in galaxies have been confined to very small samples and have yielded inconclusive results (e.g. Wong, Blitz & Bosma 2004; Haan et al. 2009; Zhang & Buta 2012). Difficulties arise from the fact that flow patterns in individual galaxies are often irregular and disks are frequently not axisymmetric. In addition, different methods for estimating mass inflow rates yield discrepant results.

As a result, modellers generally resort to simple parameterized inflow prescriptions (e.g Lacey & Fall 1985; Portinari & Chiosi 2000; Schönrich & Binney 2009; Spitoni & Matteucci 2011). In this work, we have tested a number of inflow prescriptions. We first tried the simplest prescription in which the radial gas inflow velocity is constant for the whole disk (model (a) in Lacey & Fall 1985), but we found that the inflow velocities required to move enough gas from the outer disk to the inner disk to compensate the depletion by star formation, lead to an unacceptably large pile-up of gas in the very inner disk. A prescription in which the rate of change of the angular momentum is proportional to the angular momentum yields results that agree best with observational data, i.e

$$\frac{dL_{\text{gas}}}{dt} = C L_{\text{gas}} \quad (9)$$

where C is a constant for all galaxies. Because $L_{\text{gas}} = m_{\text{gas}} r_{\text{gas}} v_{\text{cir}}$, we have that

$$v_{\text{inflow}} = \alpha_v r \quad (10)$$

The radial inflow velocity of the gas is thus proportional to the galactocentric radius r . This is equivalent to model (b) in Lacey & Fall (1985). Spitoni & Matteucci (2011) also invoke a radial flow prescription of this form to reproduce the observed stellar metallicity gradient in the Milky Way.

The constant α_v in Eq. (10) is an adjustable model parameter. As discussed later, $\alpha_v = 0.7 \text{ km s}^{-1} \text{ kpc}^{-1}$ is required to fit observations. This results in negligible flow velocities in the inner disk and flow speeds of several km s^{-1} in the outer disk (see Fig. 1).

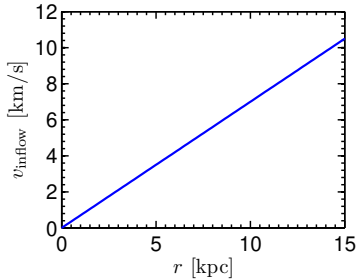


Figure 1. The relation between galactocentric radius r and radial gas inflow velocity v_{inflow} from Eq. (10) ($\alpha_v = 0.7 \text{ km s}^{-1} \text{ kpc}^{-1}$ is adopted).

In the models, we calculate the gas inflow velocity according to Eq. (10) after processing gas cooling and infall in each time step and derive the new radius $r' = r - v_{\text{inflow}} \Delta t$ for the gas in each ring, where Δt is the length of the time step. Proceeding from the inner ring to the outer ring, we move the gas to its new radius; metals associated with the cold gas move inward together with the gas.

In Fig. 2, we show the best-fit radial surface density profiles of stars, atomic gas, molecular gas, and total cold (atomic+molecular) gas for disk galaxies in haloes with circular velocities comparable to that of the Milky Way ($200 < v_{\text{circ}} < 235 \text{ km/s}$) at $z = 0$. The four panels on the left show the results if radial gas inflows are not included, and the four right panels show the results of our inflow model. Without inflows, both the molecular gas and average total cold gas radial surface density profiles are too flat in comparison to the data of Leroy et al. (2008). The right panels show that the inclusion of radial flows leads to gas profiles that are in much better agreement with observations. We note that the stellar mass profiles are insensitive to the radial flow prescription; this is because the majority of the mass in the inner galaxy forms at high redshifts from gas cooling in smaller, denser haloes. The gas radial profiles are set by gas that cools at late times. Because the timescale over which H_2 is transformed into stars is $\sim 2 \text{ Gyr}$ (see next section), the H_2 surface densities in the inner disk quickly drop to low values as a result of star formation and SN feedback, unless gas is transported from the outer disk to the inner regions of the galaxy.

We note that we have tuned the parameters of the radial inflow model (in particular the constant α_v in Eq. 10) so that the gas radial profiles in Milky Way-type disks are reproduced. One might ask whether metallicity profiles provide an additional check on the inflow model. In Fig. 3, we show the mean radial gas-phase metallicity profile (left panel) and stellar metallicity profile (right panel) for the same set of Milky Way type galaxies at $z = 0$. Green curves show results with radial inflow and blue curves show models without radial gas inflow. In the left panel, the black dots represent oxygen metallicity measurements from HII regions in the Milky Way by Rudolph et al. (2006) and black dashed line is the corresponding linear fit to the data between 0 and 15 kpc. In the right panel, the black dots represent the stellar oxygen measurements gradients derived from Cepheids by Andrievsky et al. (2002a,b,c;2004) and Luck et al. (2003). Red dots with error bars are the corresponding mean values. As we will discuss in the next section, the prescription

for the radial inflow of gas has a much weaker influence on metallicity gradients than the fraction of the metals produced by SNe we choose to put into the hot gas rather than the cold interstellar medium. We see from Fig. 3 that inclusion of radial gas inflow yields stellar metallicity gradients that are slightly steeper in the region of the disk interior to 3 kpc, but otherwise the predicted metallicity gradients are virtually indistinguishable in the two cases. We note that the Spitoni & Matteucci (2011) claim that radial inflows are required to explain the observed metallicity gradients in the Milky Way, but in their models accreted gas always has primordial metallicity. In our model, infalling gas from the halo has already been pre-enriched by the ejection of metals during the early formation phase of the galaxy.

2.4 Star formation prescription

In this paper, we adopt a simple law in which the star formation surface density is proportional to the H_2 surface density: $\Sigma_{\text{SFR}} \propto \Sigma_{\text{H}_2}$ (e.g Leroy et al. 2008; Bigiel, Leroy & Walter 2011; Schruba et al. 2011; Leroy et al. 2013). We adopt a constant molecular gas consumption timescale for all galaxies at all redshifts. There is evidence that molecular gas consumption times may be longer in massive, early-type galaxies than in normal, present-day star-forming spirals (Saintonge et al. 2011b) and shorter in starburst galaxies (Genzel et al. 2010), but we will neglect these complications, because it is still unclear what the underlying physical cause of these effects are.

The star formation law adopted in the model can be simply written as

$$\Sigma_{\text{SFR}} = \alpha_{\text{H}_2} \Sigma_{\text{H}_2} \quad (11)$$

in which the H_2 star formation efficiency $\alpha_{\text{H}_2} = 5.3 \times 10^{-10} \text{ yr}^{-1}$ is slightly adapted to yield a better fit to the results stellar mass function at $z = 0$. We note that the molecular gas surface density Σ_{H_2} in Eq. (11) does not include the helium component.

2.5 Prescriptions for the transition between atomic and molecular gas in the ISM

In Fu10, we implemented two prescriptions for the transition between atomic and molecular gas in the interstellar medium. One is from Krumholz et al. (2009) (H_2 fraction prescription 1), who calculate an equilibrium H_2 fraction for a spherical cloud with given dust content surrounded by a photo-dissociating UV field. In this prescription, the H_2 fraction is primarily a function of local cold gas surface density and metallicity. The second prescription originates from Elmegreen (1989, 1993) and Blitz & Rosolowsky (2006), in which the H_2 fraction is a function of the pressure in the ISM. We adopt the approximation by Obreschkow & Rawlings (2009), in which the local ISM pressure is expressed as a function of gas and stellar surface density in the radial ring. More details can be found in Section 3.2 of Fu10.

In this paper, we make a number of adaptations to the Krumholz et al. prescription. We update the prescription using the recent fitting equations in McKee & Krumholz (2010) with the molecular gas fraction f_{H_2} given by

$$f_{\text{H}_2} = 1 - \frac{3}{4} \frac{s}{1 + 0.25s} \quad (12)$$

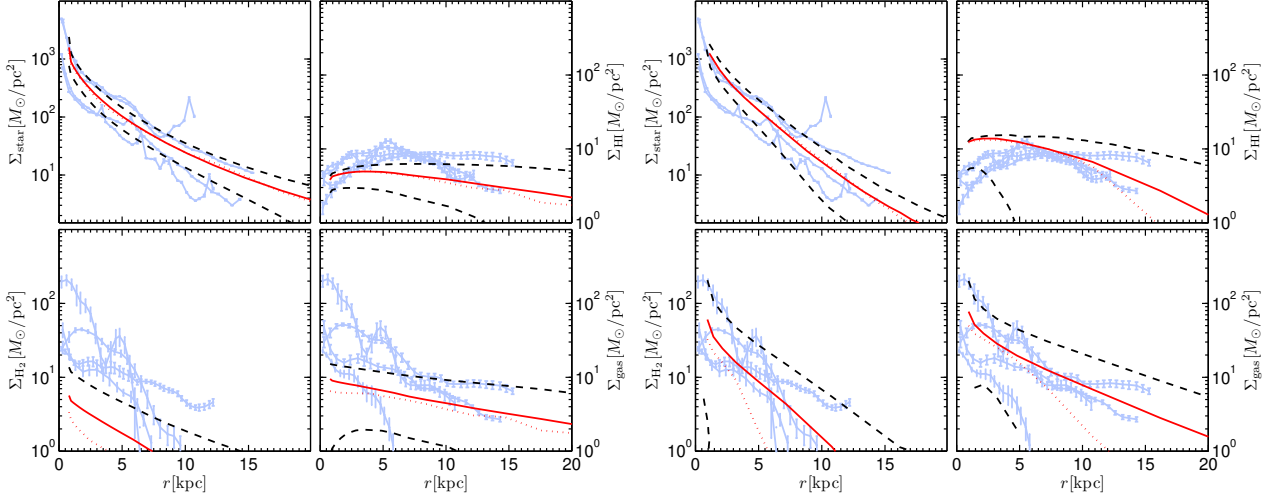


Figure 2. The radial surface density profiles of stars, atomic gas, molecular gas, and total cold gas for disk galaxies similar to the Milky Way. Results from the model with H_2 fraction prescription 1 are shown at $z = 0$. The two panels show the model results with (right panel) and without (left panel) radial gas inflow. The light blue curves with error bars are taken from the data of Leroy et al. (2008) for disk galaxies in the range of circular velocities $200\text{kms}^{-1} < v_{\text{cir}} < 235\text{kms}^{-1}$ (NGC 0628, NGC 3184, NGC 5194, NGC 3521). The red solid and dotted curves are the mean and the median values from model results, and the black dashed curves are the $\pm 1\sigma$ deviations about the mean values.

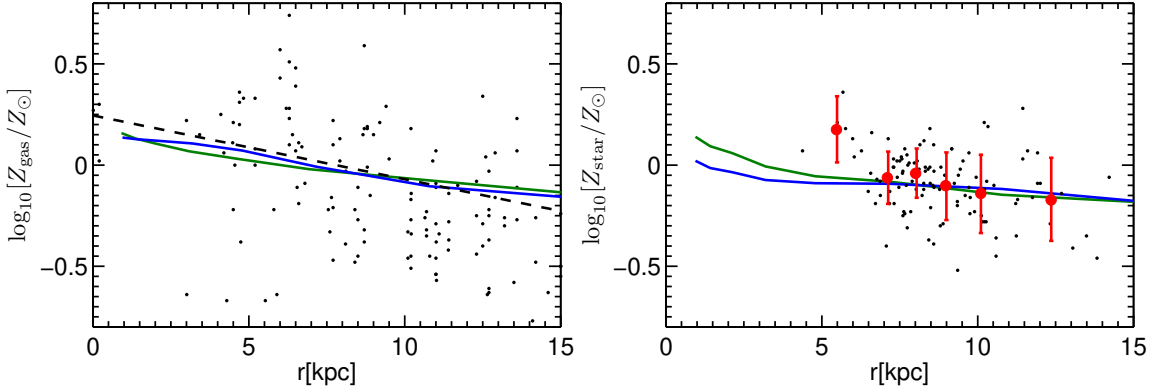


Figure 3. The mean radial metallicity profile of gas (left panel) and stars (right panel) for a Milky Way-sized galaxy at $z = 0$ from models with (green curve) and without (blue curve) radial gas inflow. In the left panel, the black dots are the oxygen metallicity from HII regions in the Milky Way (Rudolph et al. 2006) and black dashed line is the corresponding linear fit to the data between 0 and 15 kpc. In the right panel, the black dots represent the stellar oxygen gradients from Cepheids (Andrievsky et al. 2002a,b,c; 2004; Luck et al. 2003) and the red dots with error bars are corresponding mean values.

for $s < 2$ and $f_{\text{H}_2} = 0$ for $s \geq 2$. The s in Eq. (12) is defined as

$$s = \frac{\ln(1 + 0.6\chi + 0.01\chi^2)}{0.6\tau_c} \quad (13)$$

in which $\chi = 3.1(1 + 3.1Z^{0.365})/4.1$ and $\tau_c = 0.66(\Sigma_{\text{comp}}/M_{\odot}\text{pc}^{-2})Z'$. Note that $Z' = Z_{\text{gas}}/Z_{\odot}$ is the gas-phase metallicity relative to the solar value, and Σ_{comp} is the gas surface density of the giant gas cloud. Since the gas surface density in the model is the azimuthally averaged value in each concentric ring, a clumping factor c_f is introduced to consider the difference between Σ_{comp} and Σ_{gas}

$$\Sigma_{\text{comp}} = c_f \Sigma_{\text{gas}} \quad (14)$$

One problem with the Krumholz et al. prescription is that it can easily yield non-convergent results. The reason for this is that the value of f_{H_2} is very sensitive to the ex-

act value of the gas-phase metallicity when the metallicity is well below the solar value (see Figure 5 in McKee & Krumholz 2010). Molecular clouds do not form until metals have been produced, and metal production is dependent on the formation of stars, which can only take place in molecular clouds, so the conditions for star formation to occur in the first generation of haloes to form in the simulation are subject to considerable uncertainty. Moreover, at the resolution limit of the simulation, the assembly histories of haloes, and hence the star formation histories of galaxies embedded within them, cannot be tracked accurately. It thus becomes very difficult to get results that are consistent for galaxies forming in haloes of the same mass in simulations of different resolutions (e.g. MS and MS-II). Similar problems were reported by Kuhlen et al. (2012) in their attempts to model dwarf galaxies with Krumholz et al. prescription.

In the top panels of Fig. 4, we plot the relation between

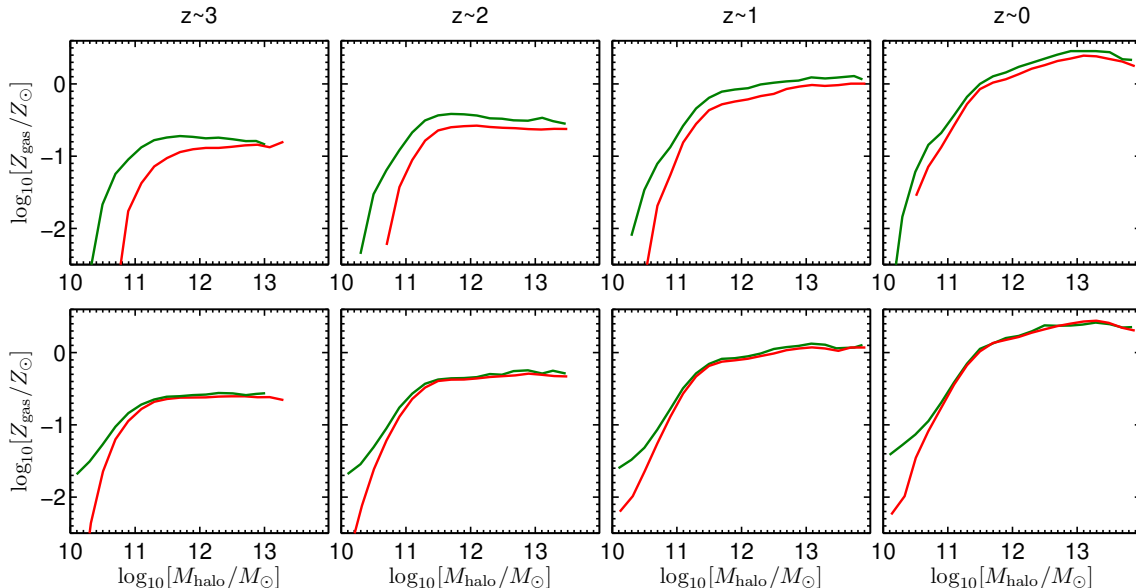


Figure 4. The relation between gas phase metallicity and galaxy halo mass at redshifts 3, 2, 1, and 0. The red curves and green curves are the mean values derived for the MS and the MS-II simulations, respectively. The four top panels are from the Krumholz et al. H_2 prescription with fixed clumping factor $c_f = 1.5$, and the four bottom panels are from the Krumholz et al. H_2 prescription with variable clumping factor dependent on gas-phase metallicity (see text).

the gas-phase metallicity of a central galaxy and the mass of its parent halo at different redshifts. The red curves and green curves show results for the MS and MS-II simulations, respectively. We have adopted $c_f = 1.5$ for all galaxies at all redshifts, as in Fu10. As can be seen, at fixed halo mass, the gas-phase metallicity is higher in the MS-II run than in the MS run, particularly for low mass haloes at high redshifts. Since the halo resolution of MS-II is 125 times higher than MS, a larger fraction of the formation and chemical enrichment history of low mass haloes lies below the resolution limit for MS than MS-II. Because the Krumholz et al. prescription is so sensitive at low metallicities, the resolution discrepancies are enhanced for high redshift galaxies in low mass haloes.

The question arises as to why stars are able to form at all in low-metallicity galaxies. For example, 1ZW18 is the most metal-poor galaxy known, yet it is a starburst system (e.g. Martin 1996). The main reason is that the gas in low-metallicity dwarf galaxies is clumpy on scales of ~ 100 pc (Lo, Sargent & Young 1993; Stil & Israel 2002). To account for this, Kuhlen et al. (2012) adopt a clumping factor $c_f = 30$ for their models of dwarf galaxies at high redshift; Luo et al. (2011) adopt $c_f = 20$ to model high-redshift damped Lyman-alpha systems.

In this paper, we adopt a variable clumping factor that depends on gas-phase metallicity. We use the following equation to describe the relation between gas-phase metallicity and clumping factor

$$c_f = Z'^{-0.7} \quad (15)$$

for $0.01 < Z' < 1$ and $c_f = 1$ for $Z' \geq 1$. The clumping factor for $\log_{10} Z' > -1$ is between 1 and 5, which agrees with the values suggested for normal galaxies in KMT09.

In the four bottom panels of Fig. 4, we plot central galaxy gas-phase metallicity as a function of halo mass for

models that adopt a variable c_f . Interestingly, the difference between MS-I and MS-II results is largely eliminated for galaxies in haloes with larger than $10^{11} M_\odot$, because the higher clumping factor compensates the low molecular gas surface densities in dwarf galaxies and high redshift galaxies with low gas-phase metallicities. Of course, this does not mean that our clumping factor prescription is correct! It just means that we are able to match together the results from the two simulations with greater ease.

2.6 The mixing of metals

In the models of DLB07, Guo11 and Fu10, metals produced by star formation in the disk are mixed instantaneously with the cold gas in the disk. SN reheating results in part of the cold gas (along with the metals that have been mixed into it) being transferred to the hot gas in the halo. If the SN explosion energy E_{SN} is larger than the energy required to reheat the cold gas E_{reheated} , the remaining energy $E_{\text{SN}} - E_{\text{reheated}}$ will eject part of the halo hot gas out of the halo: this corresponds to the so-called “ejected component”.

We note, however, that there is direct observational evidence from deep X-ray spectral imaging of nearby star-forming disk galaxies that the hot gas produced by SNII is highly metal-enriched (Martin, Kobulnicky & Heckman 2002) and also enhanced in alpha elements (Strickland et al. 2004). Even in “normal” spirals, the gas is directly observed at scale heights 4-8 kpc above the galactic disk, before its emissivity decreases below the detection threshold (Strickland et al. 2004). The scenario favoured by current observations is that SN feedback in the disks of star-forming galaxies create exponential atmospheres of hot gas via blow-out and venting of hot gas from the disk.

We have experimented with mixing a fraction $f_{z,\text{hot}}$ of the metals produced by star formation directly with the hot

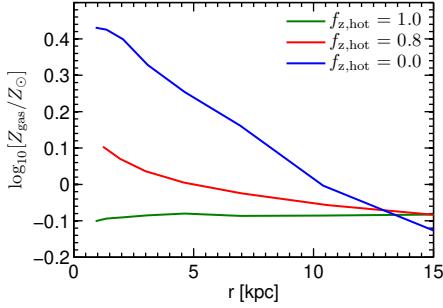


Figure 5. The radial gas-phase metallicity gradient for Milky Way sized galaxies from the model results at $z = 0$. The 3 different colour curves represent the model results with $f_{z,\text{hot}} = 0.0, 0.8, 1.0$, respectively.

gas in the halo. This turns out to have very strong impact on the predicted gas-phase metallicity gradients in the galaxy. In Fig. 5, we plot the mean radial gas-phase metallicity gradients for Milky Way-type galaxies at $z = 0$. The blue curve shows results for $f_{z,\text{hot}} = 0.0$, which is effectively the DLB07 and Guo11 mixing prescription, in which none of the metals are directly mixed into the hot gas. This yields a steep gradient, with more than 0.6 dex change in metallicity in the inner 15 kpc of the galaxy. The green curve shows what happens if we adopt $f_{z,\text{hot}} = 1.0$, i.e. all metals are mixed with the hot gas. In this case, the metallicity gradient nearly disappears, because we assume the hot gas in the halo is fully mixed and the infalling gas onto the disk has a uniform metallicity at different radii. According to the yield data compiled by Marigo et al. (2001) for a Kroupa IMF, about 20 percent of the total metal yield comes from AGB stars of low and intermediate masses. The red curve in in Fig. 5 shows the case where metals from AGB star outflows are retained in the cold ISM and metals from core-collapse SN explosions are mixed into hot gas ($f_{z,\text{hot}} = 1 - 0.2 = 0.8$).

In Sec. 5, we will compare the model gas-phase metallicity gradients to observations and also explore how the predicted metallicity profiles depend on galaxy properties such as mass and gas mass fraction. We will show that $f_{z,\text{hot}} = 0.8$ gives reasonably good agreement with observations.

2.7 The parameters in the models

As discussed in Fu10, we tune the model parameters to fit the observed stellar, HI and H₂ mass functions at $z = 0$. In the top part of Tab. 1, we list the model parameters which change in this paper with respect to those listed in previous papers. The value of H₂ star formation efficiency α_{H_2} , the amplitude of SN reheating efficiency ϵ , and the quiescent hot gas black hole accretion rate κ are tuned to fit the amplitudes of both the stellar and the gas mass functions. The normalization of the radial gas inflow rate α_v in Sec. 2.3.3 is tuned to reproduce the gas surface density profiles of Milky Way-type galaxies and to fit the observed HI and H₂ mass functions. The fraction of metals directly mixed with halo hot gas is chosen to be 0.8. Other parameters are the same as in previous papers (bottom section of Tab. 1): f_b , f_{BH} , T_{merger} , Y are the same as in Table 1 in Croton et al. (2006) (they remain unchanged in DLB07, Fu10, Guo11 and Guo13); R is same as in DLB07 (it remains unchanged

in Guo11 & Guo13); β_1 , V_{reheat} , η , β_2 , V_{eject} are same as in Table 2 in Guo13; γ is the same as in Table 1 in Guo11 (it remains unchanged in Guo13); ξ , P_0 , α_P are the same as in Table 1 of Fu10.

3 STELLAR AND GAS MASS FUNCTIONS AT $Z = 0$

The Fu10 models use the SN feedback prescriptions in DLB07, resulting in stellar, HI and H₂ mass functions that are too steep at low masses (see Figure 1 in Fu et al. 2012). In this paper, we use the prescriptions in Guo11, which provide a better fit to the low-mass end of the stellar mass function.

In Fig. 6, we show the mass functions of stars, molecular gas and atomic gas for our revised models. Red solid curves show results for H₂ fraction prescription 1 and green solid curves for H₂ fraction prescription 2. We have computed the mass functions using the combined results from running the code on the MS and MS-II simulations. Blue circles show the stellar mass function derived from the Data Release 7 of SDSS by Li & White (2009); black diamonds show SDSS Data Release 4 results from Baldry et al. (2008). The observed H₂ mass function was derived from the FCRAO survey (Young et al. 1995) assuming a constant CO-H₂ conversion factor by Keres, Yun & Young (2003). The HI mass functions are from Zwaan et al. (2005) (blue circles) and Martin et al. (2010) (black diamonds).

As mentioned in Sec. 2.7, we tune the model parameters to fit the HI, H₂ and stellar mass functions, so it is no surprise that the agreement with models is very good.

4 STAR FORMATION GRADIENTS

In this section, we compare the star formation rate gradients in our model galaxies with observations. This provides an important test of whether the present-day growth of disks predicted by the models agrees with the data.

We have adopted two observational samples for the analysis. Leroy et al. (2008) analyzed star formation gradients in a sample of 23 nearby spiral galaxies from the THINGS/HERACLES survey, finding that the scale length of the star formation rate surface density profile l_{SFR} is roughly proportional to the scale length of the stellar disk l_* ($l_{\text{SFR}} = (1 \pm 0.2)l_*$). We also make use of star formation rate surface density measurements from the MMT long-slit observations of 174 galaxies from Moran12. 119 of these galaxies (i.e. around 70% of the total sample) have emission lines strong enough to measure both SFR and gas-phase metallicity gradients out to $2r_{50}$.

In Fig. 7, we plot the star formation rate surface density as a function of scaled radius for model galaxies in four different stellar mass bins: $9.0 < \log_{10}[M_*/M_\odot] < 9.5$, $9.5 < \log_{10}[M_*/M_\odot] < 10.0$, $10.0 < \log_{10}[M_*/M_\odot] < 10.5$, and $10.5 < \log_{10}[M_*/M_\odot] < 11.0$. For the model sample, r_d is calculated by fitting exponentials to the stellar profiles of the disk. The red solid and green dashed curves show results of mean radial profiles for H₂ fraction prescriptions 1 and 2, respectively, and the error bars on the red solid curves represent the $\pm 1\sigma$ scatter between different model galaxies.

Table 1. The model parameters introduced/changed in this paper (top section) and other parameters whose values are the same as in previous papers (bottom section). Note that the parameters marked as “Croton et al. (2006)” remain unchanged in DLB07, Fu10, Guo11 and Guo13.

| Parameter | Value | Description | Remark |
|-----------------------|--|---|-----------------------------------|
| α_v | $0.7 \text{ km s}^{-1} \text{ kpc}^{-1}$ | the ratio of radial gas inflow and gas radius | Eq. (10) |
| α_{H_2} | $5.3 \times 10^{-10} \text{ yr}^{-1}$ | H_2 star formation efficiency | Eq. (11) |
| ϵ | 5.0 | Amplitude of SN reheating efficiency | Tab. 1 in Guo11 & Tab. 2 in Guo13 |
| κ_{AGN} | $1.5 \times 10^{-5} M_{\odot} \text{ yr}^{-1}$ | Quiescent hot gas black hole accretion rate | |
| $f_{z,\text{hot}}$ | 0.8 | Fraction of metal elements from quiescent star formation directly mixed with halo hot gas | Sec. 2.6 |
| f_b | 0.17 | Cosmic baryon fraction | Croton et al. (2006) |
| f_{BH} | 0.03 | Merger cold gas BH accretion fraction | Croton et al. (2006) |
| T_{merger} | 0.3 | Major merger mass ratio threshold | Croton et al. (2006) |
| Y | 0.03 | Yield of metals produced per unit star formation | Croton et al. (2006) |
| R | 0.43 | Instantaneous recycled fraction of star formation to the cold gas | DLB07, Guo11 & Guo13 |
| β_1 | 3.2 | Slope of SN reheating efficiency | Guo13 |
| V_{reheat} | 80 km s^{-1} | Normalization of SN reheating efficiency | Guo13 |
| η | 0.18 | Amplitude of SN ejection efficiency | Guo13 |
| β_2 | 3.2 | Slope of SN ejection efficiency | Guo13 |
| V_{eject} | 90 km s^{-1} | Normalization of SN ejection efficiency | Guo13 |
| γ | 0.3 | Ejecta reincorporation efficiency | Guo11 & Guo13 |
| ξ | 1.3 | Warm-phase correction factor | Fu10 |
| P_0, α_P | $5.93 \times 10^{-13} \text{ Pa}, 0.92$ | Constant and index of the relation between molecular ratio and ISM pressure | Fu10 |

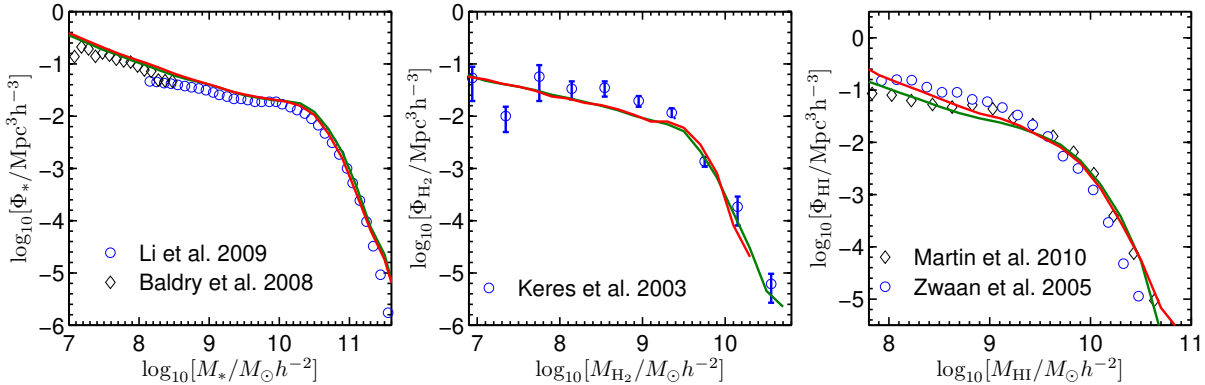


Figure 6. The stellar, H_2 and HI mass functions from model galaxies at $z = 0$ compared with the observations. The red solid curves and green solid curves in each panel are from the models with H_2 fraction prescription 1 and 2, respectively. The observed stellar mass functions are from Li & White (2009) and from Baldry et al. (2008). The observed H_2 mass function is from the FCRAO CO survey by Keres et al. (2003). The observed HI mass function is from Zwaan et al. (2005) using HIPASS data, and Martin et al. (2010) using ALFALFA data.

In each panel, black curves with error bars are star formation surface density profiles from Leroy et al. (2008); r_d for each galaxy is taken from Table 4 of that paper. The light blue dots are from Moran12, who obtained long-slit spectra of 174 star-forming galaxies with stellar masses greater than $10^{10} M_{\odot}$ from the GALEX Arecibo Sloan Digital Sky Survey (GASS) survey (Catinella et al. 2010). In this case, r_d is estimated from r_{90} assuming an exponential profile (i.e. $r_{90} = 3.9r_d$). Note that we have simply plotted the star formation rate surface density measured for each spectral bin along the slit, i.e. these data points are not averaged in radial bins as for the Leroy et al. data, so the scatter from one galaxy to another will be substantially larger. The grey shaded region shows the 1σ scatter around the median for

the Moran12 sample. As can be seen, the agreement between the Moran et al. and the Leroy et al. data is quite good.

Our results for H_2 fraction prescription 1 agree well with the data, particularly for the 3 highest stellar mass bins. H_2 fraction prescription 2 yields higher star formation rate surface densities in the outer disks. This is because the pressure-based prescription yields higher H_2 fractions in regions of low gas surface density with low gas-phase metallicities.

We note that we tuned the radial inflow prescriptions to match the H_2 surface density profiles of the galaxies in the Leroy et al. sample for stellar masses $\log_{10}[M_*/M_{\odot}] \sim 10.6$. Our star formation prescription is also motivated by results obtained for this sample. This means that star

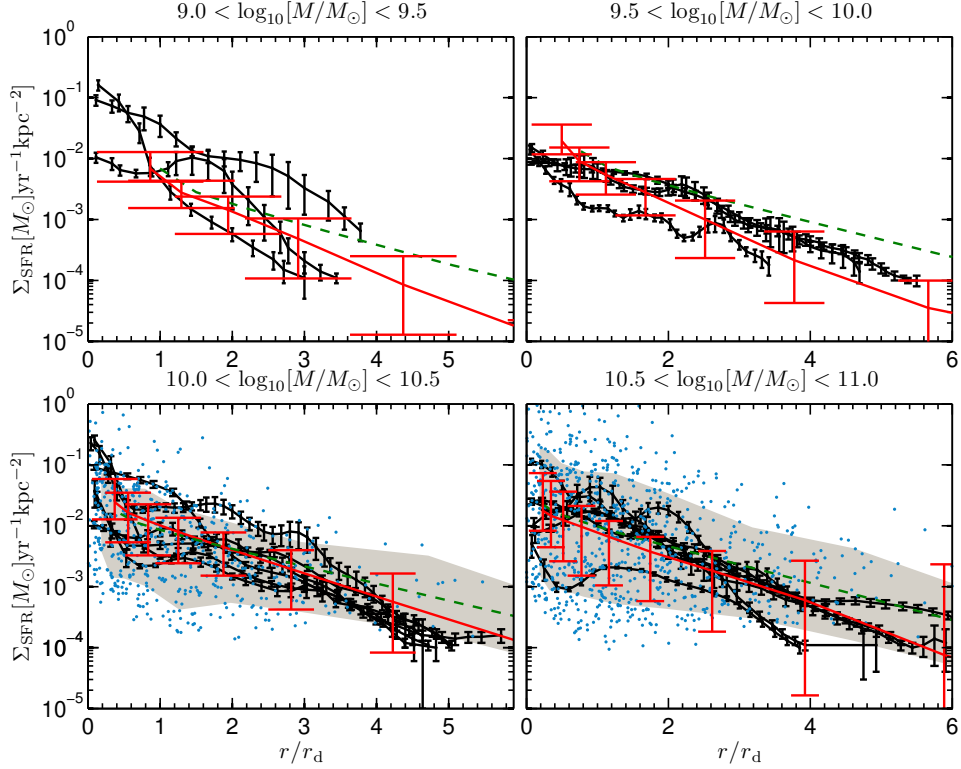


Figure 7. The radial profiles of star formation surface density for model galaxies at $z = 0$ compared with observations from Leroy et al. (2008) (black curves with error bars) and Moran12 (blue dots). The gray areas represent the $\pm 1\sigma$ deviations around the median values for the Moran12 data. The red solid curves show model results of mean radial profiles for H_2 prescription 1 and the green dashed curves are for H_2 fraction prescription 2. The error bars on the red solid curves represent $\pm 1\sigma$ scatter about the mean values for the model. The panels show results in 4 stellar mass bins: $10^{9.0} < M_*/M_\odot < 10^{9.5}$, $10^{9.5} < M_*/M_\odot < 10^{10.0}$, $10^{10.0} < M_*/M_\odot < 10^{10.5}$, $10^{10.5} < M_*/M_\odot < 10^{11.0}$. The radii plotted on the x-axis are scaled by dividing by the disk scale length r_d .

formation rate surface density profiles for galaxies with $\log_{10}[M_*/M_\odot] \sim 10.6$ will match the data, essentially by construction. The main check in this section is to test whether we can match to SFR profiles over a large range in stellar mass. One significant conclusion that we reach is that H_2 fraction prescription 1 does a better job than H_2 prescription 2 at matching the outer gas profiles of galaxies with stellar masses less than $10^{10} M_\odot$.

5 GAS-PHASE METALLICITY GRADIENTS IN GALAXIES

In this section, we will compare the gas-phase metallicity gradients predicted by the model with data from Moran12. We will first study how the gradient depends on the stellar mass of the galaxy, and then examine its dependence on the global gas fraction. When we compare the model with data from Moran12, we choose galaxies that have HI and H_2 gas mass fractions greater than $\sim 1 - 3\%$, such that HI and CO lines would be detected in the GASS and COLD GASS surveys: i.e. $\log_{10}[M_{\text{HI}}/M_*] > -1.82$ for galaxies with $\log_{10}[M_*/M_\odot] > 10.3$, and $\log_{10}[M_{\text{HI}}/M_*] > -1.066 \log_{10}[M_*/M_\odot] + 9.16$ for galaxies with $10.0 < \log_{10}[M_*/M_\odot] < 10.3$ (Kauffmann et al. 2012). This is a slightly more stringent cut than adopted by Moran12 for his emission-line analysis, but we have verified that the pre-

cise location of the cut makes negligible difference to all the results presented in this paper.

We adopt the gas phase oxygen abundance based on the O3N2 empirical index described by Pettini & Pagel (2004), which is derived from the $\text{N}[\text{II}]\lambda 6583/\text{H}\alpha$ and $\text{O}[\text{III}]\lambda 5007/\text{H}\beta$ emission line ratios (see Section 3.1 of Moran12 for more details).

In the models, we only track total metallicity; the value of Z_{gas}/Z_\odot represents the cold gas-phase metallicity in units of the solar value. To make a comparison to oxygen abundance from observations, we adopt $12 + \log_{10}(\text{O}/\text{H}) = 8.69$ as the solar value (Asplund et al. 2009). We convert Z_{gas} to $(\text{O}/\text{H})_{\text{gas}}$ using the equation

$$12 + \log_{10}(\text{O}/\text{H})_{\text{gas}} = \log_{10}[Z_{\text{gas}}/Z_\odot] + 8.69 \quad (16)$$

5.1 Gas-phase metallicity gradients as a function of stellar mass

In Fig. 8, we plot mean gas-phase metallicity profiles for model galaxies in 3 stellar mass bins: $10^{9.5} < M_*/M_\odot < 10^{10.0}$, $10^{10.0} < M_*/M_\odot < 10^{10.5}$, and $10^{10.5} < M_*/M_\odot < 10^{11.0}$. The top two panels show results for H_2 fraction prescription 1 and the bottom two panels are for H_2 fraction prescription 2. In the left panels, metallicity is plotted as a function of radius in kpc, and in the right panels it is plotted as a function of radius scaled by r_{90} , the radius enclosing 90% of the total stellar mass of the galaxy. The main result

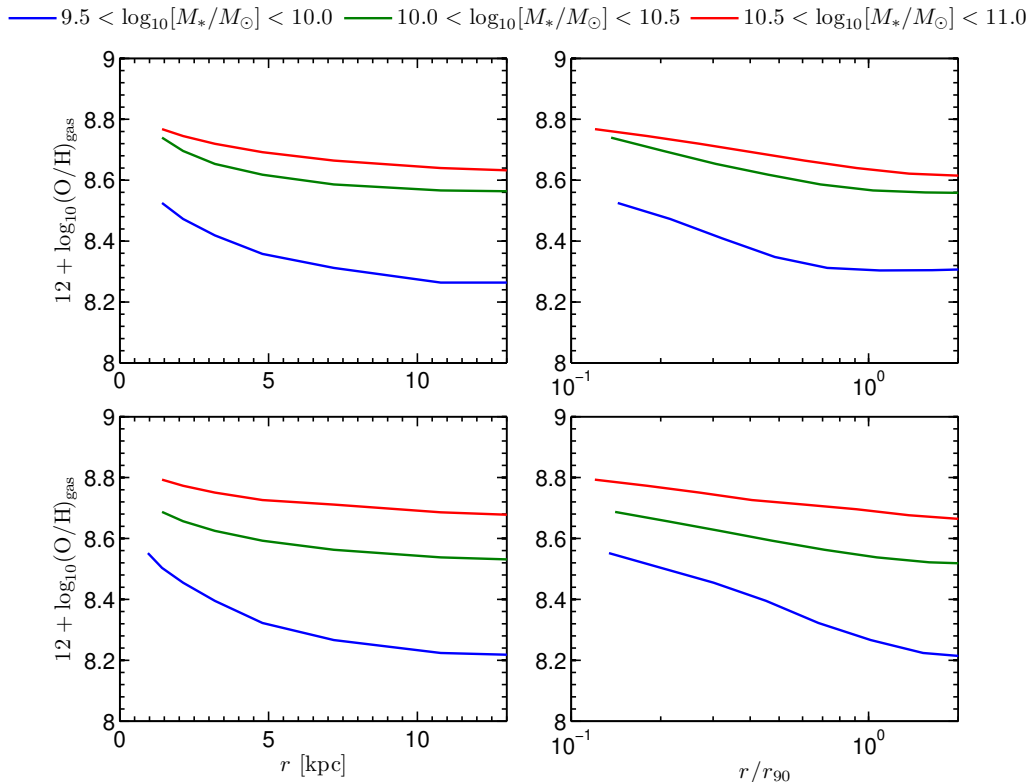


Figure 8. The mean radial profiles of gas-phase metallicity from model galaxies at $z = 0$ in 3 mass bins: $10^{9.5} < M_*/M_\odot < 10^{10.0}$ (blue), $10^{10.0} < M_*/M_\odot < 10^{10.5}$ (green), $10^{10.5} < M_*/M_\odot < 10^{11.0}$ (red). The top two panels are the results from H_2 fraction prescription 1, and bottom two panels are from H_2 fraction prescription 2. The radii plotted on the x-axis are scaled by dividing by the disk scale length r_d .

is that the gas radial metallicity profiles are flatter in higher mass galaxies; this is seen both in the left and in the right panels, where the radius has been scaled by the size of the galaxy.

We have investigated the *cause* of varying metallicity gradients in the models by examining how the metallicity gradient in a central galaxy of a given halo evolves over time. We have found that the evolution of the gas-phase metallicity gradient is most closely tied to the *merger history* of the galaxy. The starbursts induced by the mergers consume all the cold gas (in the case of major mergers) or a large fraction of it (in the case of minor mergers). The gas that later cools to form the disk has already been significantly enriched, and as a result, the gas-phase radial metallicity gradient in the new disk will be much weaker. The models thus predict that gas-phase metallicity gradients correlate more strongly with the bulge mass fraction of the galaxy than with its stellar mass. The correlation with stellar mass arises because massive galaxies have experienced more mergers and have larger bulge mass fractions than less massive galaxies.

This is illustrated in detail in Fig. 9, which shows results from models with H_2 fraction prescription 1. In the top left panel, the black solid curve shows the mean gas-phase metallicity gradient (in units of dex/r_{90}) as a function of galaxy stellar mass. The black dashed curves indicate the 1σ scatter around the mean. As can be seen, the mean gradient increases from $-0.35 \text{ dex}/r_{90}$ for galaxies with stellar masses $M_* \sim 10^{9.5} M_\odot$ to values near zero for galaxies with $M_* > 10^{10.5} M_\odot$. In the top middle panel, the gas-phase

metallicity gradient is plotted as function of bulge-to-total (B/T) mass fraction of the galaxy. A slightly stronger, and more linear correlation is seen with B/T than with stellar mass. In the top right panel, we plot the average bulge mass fraction as a function of stellar mass, which shows that more massive galaxies tend to have higher bulge mass fractions (and hence weaker metallicity gradients).

In the bottom right panel, the gas-phase metallicity gradient is plotted as a function of B/T for model galaxies in a narrow stellar mass interval ($10.0 < \log_{10}[M_*/M_\odot] < 10.2$) and in the bottom left panel metallicity gradient is plotted against M_* in a narrow interval of B/T ($0.25 < B/T < 0.3$). These two panels demonstrate that the gas-phase metallicity gradient correlates primarily with bulge mass fraction.

The purple dots superposed on the top three panels of Fig. 9 show data from Moran12. We convert the concentration index R_{90}/R_{50} measured for galaxies in this sample to a rough estimate of B/T using the fitting equation in Gadotti (2009) $R_{90}/R_{50} = 1.93 + 2.02 B/T$. Comparing the purple dots with black curves, the qualitative trends are in line with the model predictions, but the scatter is very large – once again, this is because the data points represent measurements along a 1-dimensional slit, rather than averages in radial bins as in the models. The sample is too small to investigate trends in metallicity gradient as a function of bulge fraction in a narrow stellar mass bin or as a function of stellar mass in a narrow bin of bulge-to-total ratio. It is thus not possible to assess whether the observed gas-phase metallicity gradient is more intrinsically correlated with stel-

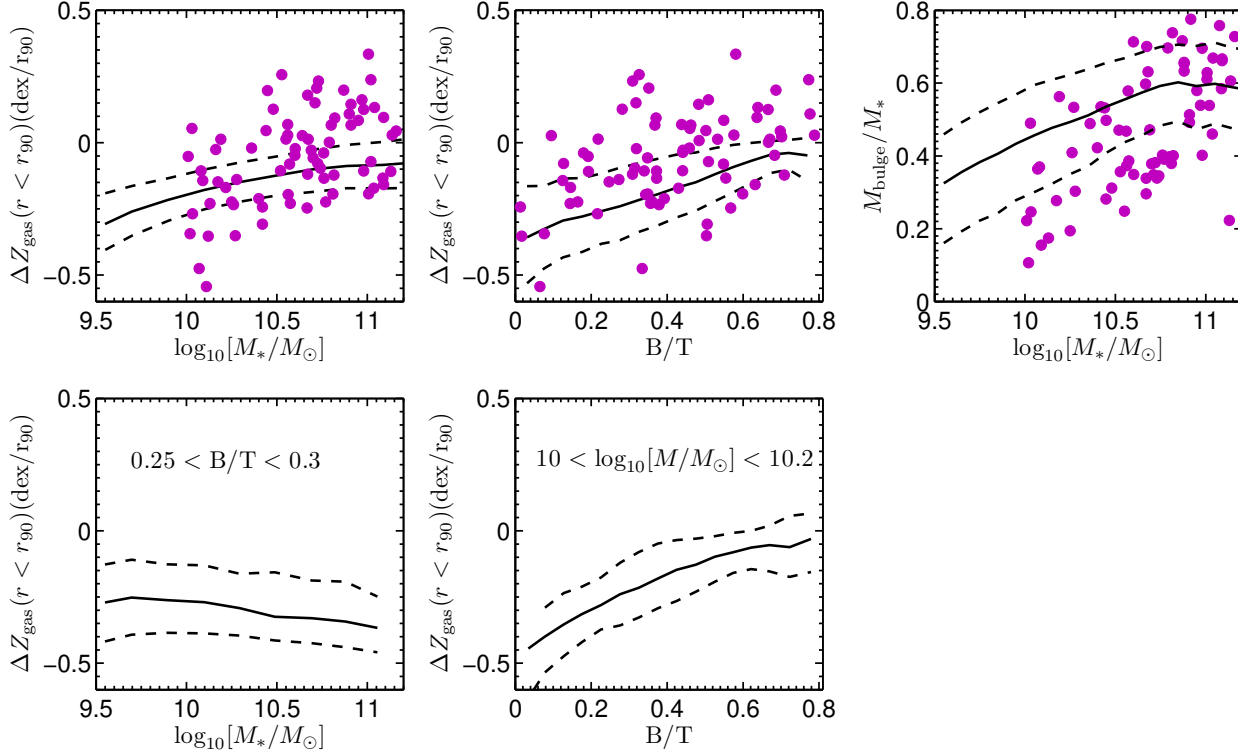


Figure 9. Top left panel: gas-phase metallicity (in units of dex/r_{90}) vs. stellar mass; top middle panel: gas-phase metallicity vs. bulge to total (B/T) ratio; top right panel: the B/T ratio vs stellar mass; bottom left panel: gas-phase metallicity vs. stellar mass for model galaxies with bulge-to-total ratio in the range $0.25 < B/T < 0.3$; bottom right panel: gas-phase metallicity vs. B/T ratio for model galaxies in the stellar mass range $10.0 < \log_{10}[M_*/M_\odot] < 10.2$. In each panel, the black solid curves show the mean values from the model sample. The black dashed curves indicate the 1σ scatter around the mean. The purple dots show the results of individual spectral bin measurements from the Moran12 data set.

lar mass of B/T . In addition, we note that there are some galaxies in the observational data set with positively sloped radial metallicity gradients. This is not seen in the models. Integral field spectroscopic observations will be required in order to ascertain whether the outliers with positive gradients are still present in similar numbers once metallicity is averaged radially.

5.2 Relations between Z_{gas} , sSFR and μ_* in the inner and the outer regions of galaxies

In this section, we will examine correlations between gas-phase metallicity, specific star formation rate and stellar mass surface density. In particular, we will ask whether these relations are the same or are different in the inner and the outer regions of galaxies. In a simple “closed-box” model, where gas is transformed into stars at a rate regulated by its density, chemical enrichment proceeds in the same way in the inner and outer regions of the galaxy. The main difference is that less gas is consumed into stars in the outer, lower density regions, resulting in lower gas-phase metallicities. In our semi-analytic models, where the inner regions of disks assemble before the outer regions, and where gas inflows and outflows regulate gas content and metallicity, star formation/metallicity correlations should be very different in the inner and outer regions of galaxies.

Moran12 examined relations between gas-phase metallicity versus specific star formation rate and stellar sur-

face mass density for spectral bins located in the inner ($R < 0.7R_{90}$) and the outer ($R > 0.7R_{90}$) regions of galaxies. It is difficult to draw clear conclusions from their analysis, because the individual spectral bin measurements in the outer regions exhibit so much scatter. In this section, we work with SFR-weighted gas-phase metallicities averaged over the inner and the outer disk, which yield considerably less scattered results. We note that the individual gas-phase metallicity measurements are well-constrained, so the scatter is a real physical effect, likely to do with longer timescales for mixing of metals in the outer disk. In our models, heavy elements injected into one radial bin are instantaneously mixed throughout that radial bin, so working with quantities that are averaged over a larger region of the disk should yield a fairer comparison. We restrict our analysis to models that use H_2 fraction prescription 1 in this section (very similar results are obtained for the other prescription). The inner disk region is defined as $r < 0.7r_{90}$, and the outer disk region as $r > 0.7r_{90}$.

In the top panels of Fig. 10, we plot the relation between SFR-weighted gas-phase metallicity and mean specific star formation rate ($\text{sSFR} = \text{SFR}/M_*$) in the inner disk (left) and in the outer disk (right). The blue dots show results for the Moran12 sample and the red and yellow contours show results for the models. We have taken care to compute the average inner and outer metallicities and sSFR in the same way in the models as in the data.

It is now clear that in the Moran12 sample, the

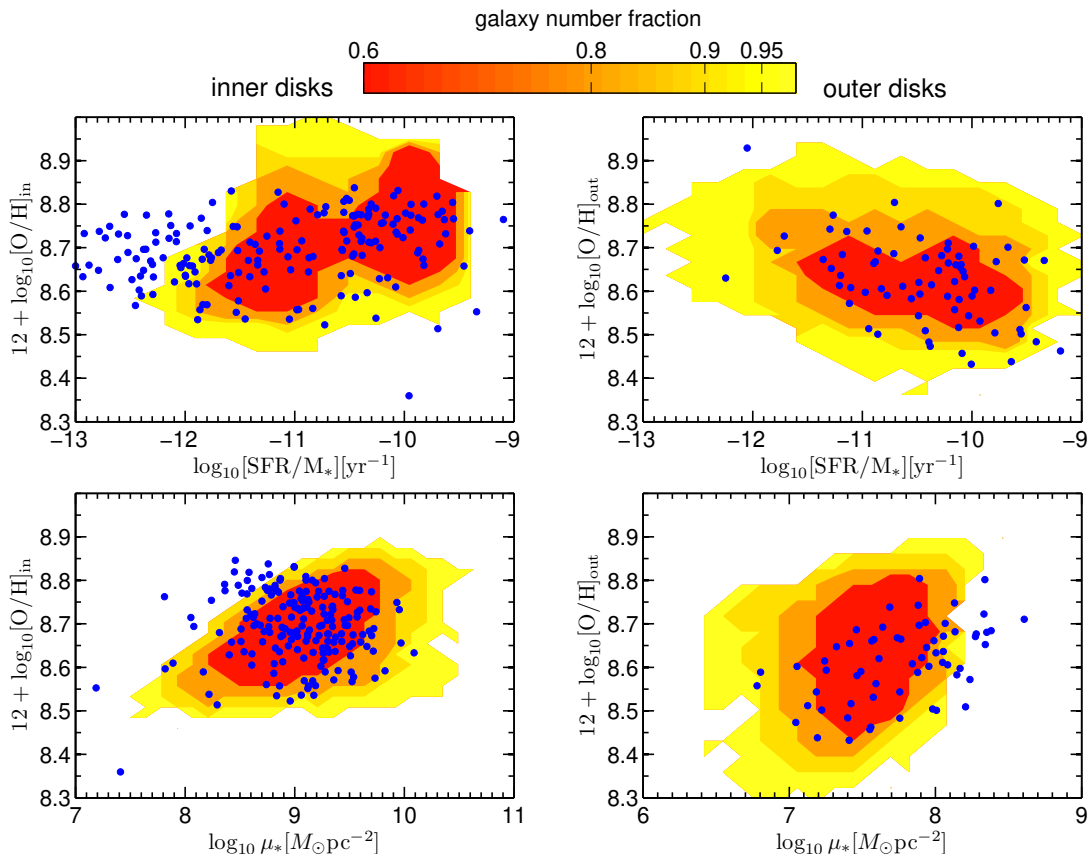


Figure 10. The relation of SFR-weighted mean metallicity vs. mean stellar mass-weighted stellar surface density μ_* and mean specific star formation rate SFR/M_* for inner and outer disks. The left two panels are the results for inner disks and right two panels are for outer disks. The blue dots are from Moran12 data and the contours indicate the fraction of model galaxies located in a given region of parameter space, as given by the colour key at the top of the plot.

metallicity-sSFR relations are quite different in the inner and the outer regions of the galaxy. At fixed sSFR, the gas-phase metallicity is systematically higher in the inner disk compared to the outer disk. The systematic offset increases towards higher values of SFR/M_* . In the inner region of the galaxy, gas-phase metallicity and SFR/M_* are weakly correlated. Regions with the highest specific star formation rates have slightly higher gas-phase metallicities. However, the opposite is true in the outer regions of the galaxy: gas-phase metallicity *decreases* at higher specific star formation rates. The data and the models agree quite well.¹

The reason for the “inverted” metallicity-sSFR relation in the outer disk can be clarified by examining the bottom two panels of Fig. 10, where we plot gas-phase metallicity as a function of mean stellar mass-weighted stellar surface mass density in the inner (left) and outer (right) regions of galaxies for both models and data. Because stellar surface density is a very steeply declining function of radius in disks (top left panels in Figure 2), the range of stellar surface densities in inner and outer disks is almost completely disjoint. In the data, gas-phase metallicity correlates with stellar sur-

face mass density only in the outer regions of galaxies, where stellar surface densities are low. In the models, there is a correlation between metallicity and μ_* in both the inner and outer regions, but it is nevertheless very much stronger in the outer disk. Our “inside-out” disk formation models predict that most of the stellar mass in the inner disk formed at high redshifts by cooling and collapse of gas within a denser progenitor halo. The outer disks are still in the process of formation at present as the halo continues to accrete dark matter and higher angular momentum gas is able to cool. The outer disks with the lowest stellar surface mass densities are found in galaxies where gas has been accreted, but has not yet reached high enough densities to form molecules and stars. The fact that the outer gas-phase metallicities in models do not reach metallicities much below 0.4 solar arises because gas that cools from the surrounding halo has been significantly pre-enriched with heavy elements (see discussion in section 6).

Finally, we would like to comment on the result in Moran12 that that around 10% of disk galaxies exhibit outer “metallicity drops”, i.e. they exhibit a sharp turndown in metallicity beyond $\sim r_{90}$. The magnitude of this drop was found to be strongly correlated with total M_{HI}/M_* ratio, but not with total M_{H_2}/M_* . We have already commented on the large scatter in metallicity from one spectral bin to another in the outer regions of galaxies in the Moran12 sample. In-

¹ We note that the sSFR can no longer be estimated at all accurately below a value of ~ -12 , so the extension of the data points to sSFR values of ~ -13 should not be regarded as a significant discrepancy.

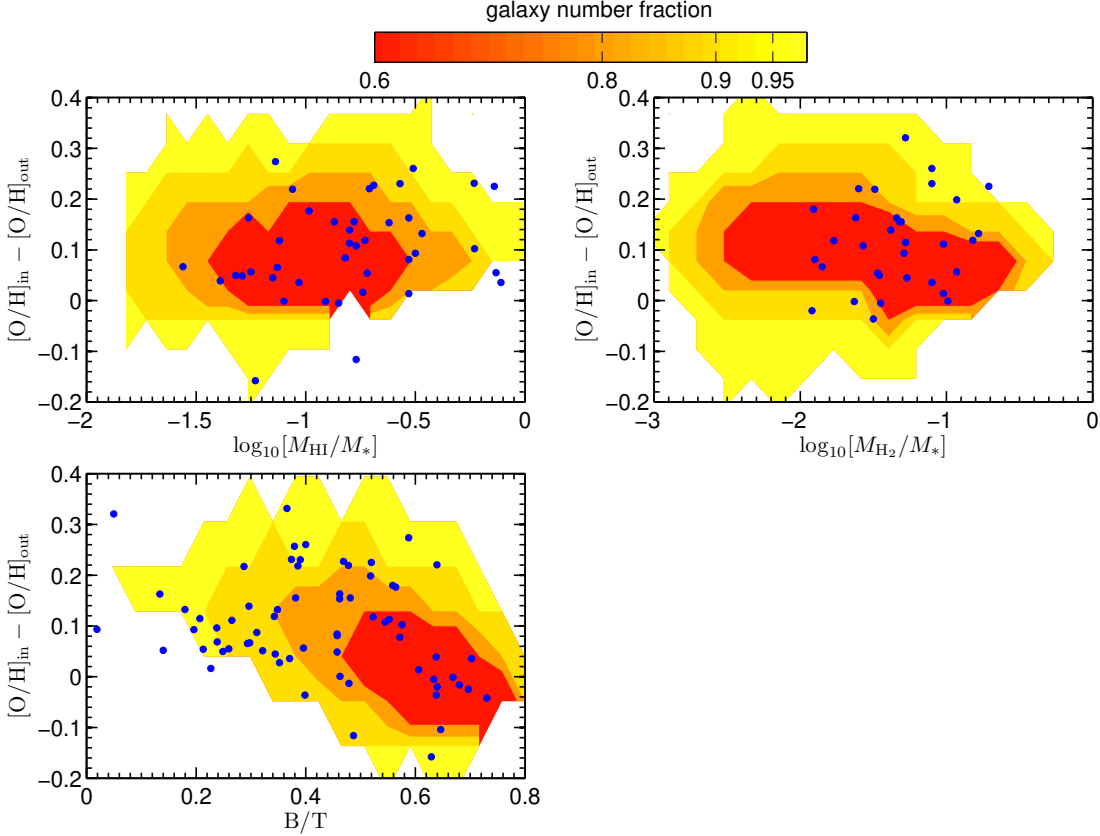


Figure 11. The relation of inner and outer disk mean gas-phase metallicity difference vs total M_{H_2}/M_* , M_{HI}/M_* and B/T ratios. The meaning of blue points and colour contour are same to those in Fig. 10.

deed, close examination of individual profiles in Figure 10 of Moran12 reveals that there is significant diversity in profile shape, even among the “metal-drop” objects.

In the top two panels Fig. 11, we examine how the inner/outer disk metallicity difference $[O/H]_{in} - [O/H]_{out}$ correlates with total M_{HI}/M_* and M_{H_2}/M_* ratios. Interestingly, for both the Moran12 data and for our model galaxies the metallicity *difference* does not correlate with either M_{HI}/M_* or M_{H_2}/M_* . This suggests that outer metallicity drops reflect the presence of *isolated* spectral bins with low metallicity. Once again integral field spectroscopy data would be extremely useful to test this conjecture in more detail. Inspired by the relation between gas-phase metallicity radial gradient vs B/T fraction in Sec. 5.1, we plot metallicity difference as a function of B/T in the bottom left panel of Fig. 11. This anti-correlation is by far the strongest one in both models and data.

6 DISCUSSION

In this paper, we describe how we have transplanted the Fu10 prescriptions for modelling the gas and stellar profiles of disk galaxies and for tracking the conversion of atomic to molecular gas to the semi-analytic model framework of Guo11. Our models are run on dark matter halo merging trees constructed from both the MS and MS-II. Each galaxy disk is divided into a series of radial concentric rings. This

allows us to track the radial distribution of gas, stars and metals in each galaxy.

The main changes with respect to the Fu10 recipes are:

- (i) We adopt a simple star formation law in which the star formation rate surface density is proportional to the molecular gas surface density $\Sigma_{SFR} \propto \Sigma_{H_2}$, rather than the two regime star formation model in Fu10.
- (ii) In Krumholz et al. H_2 prescription, we adopt a metallicity-dependent gas clumping factor so that the gas is assumed to be more clumpy in low metallicity galaxy regions. This accelerates molecule formation, star formation and metal production in low mass galaxies and in low metallicity regions and allows us to obtain convergent results in simulations with different resolutions.
- (iii) SNe feedback processes are no longer assumed to be less efficient in the regions with higher gas surface density. Instead, we include radial gas inflow so that cold gas from the outer disk moves inwards to compensate the gas consumption in the inner disk.
- (iv) The prescription for the mixing of heavy elements produced by star formation has been modified. Instead of mixing all the metals directly with the cold gas in the disk, we mix 80 % of the metals with the hot gas in the halo, and 20% of the metals with the cold gas in the disk. This partition corresponds roughly to the fraction of total metals produced by SNe as compared to AGB stars.

It is worth emphasizing which of these changes were *required* in order to fit observational data:

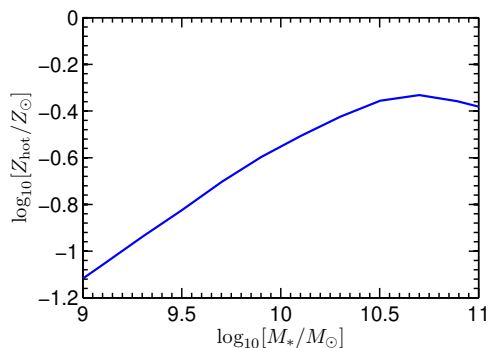


Figure 12. The mean hot gas metallicity relative to the solar value as a function of the stellar mass of the central galaxy.

Short gas consumption times in the inner disks of galaxies were already problem in the Fu10 models. In that paper, we invoked gas surface density dependent SN feedback efficiencies to prevent gas from being consumed too quickly in the inner disk. This is no longer a viable solution, because when we apply such a model to the MS II simulation, we are unable to obtain a good fit to the low mass end of the galaxy stellar mass function. This agrees with the conclusions of Guo11, who found that SN feedback efficiencies were required to be very high in low mass haloes to fit the galaxy stellar mass function at stellar masses less than few $\times 10^9 M_\odot$.

We note that the exact treatment we adopt for the radial inflow of gas has only weak influence on the gas and stellar metallicity gradients *in the outer regions of galaxies*. Outer gas-phase metallicity gradients are affected much more strongly by the fraction of metals from dying stars that is directly injected into the halo gas, rather than the interstellar medium of the galaxy. Metals ejected from a galaxy at early epochs are later re-accreted and this leads to *flatter* present-day gas-phase metallicity gradients. We demonstrate that a prescription in which 80 % of all the metals are injected into the halo gas provides the best fit to the relatively shallow observed metallicity gradients of galaxies with stellar masses greater than $10^{10} M_\odot$ (Kewley et al. 2010; Rupke et al. 2010; Moran12). We also show that such a prescription results in a good fit to the relation between gas-phase metallicity and specific star formation rate in the outer parts of galactic disks, which are still being built by gas accretion at the present day.

In Fig. 12, we plot the metallicity of the hot gas surrounding present-day central galaxies as a function of their stellar mass. As can be seen, the hot gas metallicity is predicted to increase from around 0.1 solar for central galaxies with stellar masses of $\sim 10^9 M_\odot$ to around 0.4 solar for galaxies with masses comparable to or greater than that of the Milky Way. We note that significant fraction of the hot gas around central galaxies originates from material that has been ejected out of galaxies by supernova at early epochs. In low mass haloes, SN eject most of the gas out of the halo into the so-called “ejected” component (see Figure 5 of Weinmann et al. 2010). Re-incorporation of this ejected gas into the halo occurs after a few dynamical times for a Milky Way type galaxy, but substantially longer in dwarf systems (see Equation 23 in Guo11).

The other main process that determines the strength

of the gas-phase metallicity gradient in a galaxy is bulge formation through mergers. This is because most of the gas in the galaxy is consumed when the bulge is formed, and the metallicity gradient is re-established once new gas is able to accrete. In the models, galaxies with the strongest gas-phase metallicity gradients are those that have accreted gas in an undisturbed way over the age of the Universe and that have low bulge mass fractions. We have re-examined metallicity gradient trends in the Moran12 sample and we do indeed find that the gas-phase metallicity gradient correlates more strongly with bulge-to-disk ratio than with any other property.

We caution that we have used a very simple model Eq. (10) to describe radial gas inflows and our models also neglect radial transport of gas due to bar instabilities in disks. Some observational constraints on inflows do exist (e.g Levine et al. 2006; Zhang & Buta 2012), but the measurements are often complicated by non-radial motions in individual galaxies, and average inflow measurements for galaxy samples selected by stellar mass, size, presence or absence of bars etc. are still lacking. In principle, the stellar and gas-phase metallicity profiles in the inner regions of galaxies do provide additional constraints on the inflow prescriptions (see Figure 3) and the hope is that future data sets will motivate more detailed work on this topic.

Finally, we note that the evolution of radial gas, SFR and metallicity gradients to higher redshifts is a topic that is not addressed in this paper and that may be of interest to explore in future work.

ACKNOWLEDGMENTS

We thank Bruno Henriques for discussions about the models and semi-analytic codes.

REFERENCES

- Andrievsky S. M., et al., 2002, A&A, 381, 32
- Andrievsky S. M., Bersier D., Kovtyukh V. V., Luck R. E., Maciel W. J., Lépine J. R. D., Beletsky Y. V., 2002, A&A, 384, 140
- Andrievsky S. M., Kovtyukh V. V., Luck R. E., Lépine J. R. D., Maciel W. J., Beletsky Y. V., 2002, A&A, 392, 491
- Andrievsky S. M., Luck R. E., Martin P., Lépine J. R. D., 2004, A&A, 413, 159
- Angulo, R. E., & White, S. D. M. 2010, MNRAS, 405, 143
- Asplund, M., Grevesse, N., Sauval, A. J., & Scott, P. 2009, ARA&A, 47, 481
- Avila-Reese V., Firmani C., Hernández X., 1998, ApJ, 505, 37
- Baldry, I. K., Glazebrook, K., & Driver, S. P. 2008, MNRAS, 388, 945
- Bertin G., Lin C. C., 1996, ssgd.book,
- Bigiel, F., Leroy, A., Walter, F., Brinks, E., de Blok, W. J. G., Madore, B., & Thornley, M. D. 2008, AJ, 136, 2846
- Bigiel, F., Leroy, A., & Walter, F. 2011, IAU Symposium, 270, 327
- Blitz, L., & Rosolowsky, E. 2004, ApJL, 612, L29

- Blitz, L., & Rosolowsky, E. 2006, *ApJ*, 650, 933
- Boylan-Kolchin, M., Springel, V., White, S. D. M., Jenkins, A., & Lemson, G. 2009, *MNRAS*, 398, 1150
- Bresolin, F., Ryan-Weber, E., Kennicutt, R. C., & Goddard, Q. 2009, *ApJ*, 695, 580
- Catinella, B., et al. 2010, *MNRAS*, 403, 683
- Chiappini C., Matteucci F., Gratton R., 1997, *ApJ*, 477, 765
- Cook, M., Evoli, C., Barausse, E., Granato, G. L., & Lapi, A. 2010, *MNRAS*, 402, 941
- Croton, D. J., et al. 2006, *MNRAS*, 365, 11
- Dalcanton J. J., Spergel D. N., Summers F. J., 1997, *ApJ*, 482, 659
- De Lucia, G., & Blaizot, J. 2007, *MNRAS*, 375, 2 (DLB07)
- Dutton A. A., van den Bosch F. C., Dekel A., Courteau S., 2007, *ApJ*, 654, 27
- Elmegreen, B. G. 1989, *ApJ*, 338, 178
- Elmegreen, B. G. 1993, *ApJ*, 411, 170
- Feldmann R., Hernandez J., Gnedin N. Y., 2012, *ApJ*, 761, 167
- Fu, J., Hou, J. L., Yin, J., & Chang, R. X. 2009, *ApJ*, 696, 668
- Fu, J., Guo, Q., Kauffmann, G., & Krumholz, M. R. 2010, *MNRAS*, 409, 515 (Fu10)
- Fu, J., Kauffmann, G., Li, C., & Guo, Q. 2012, *MNRAS*, 424, 2701
- Gadotti D. A., 2009, *MNRAS*, 393, 1531
- Genzel, R., et al. 2010, *MNRAS*, 407, 2091
- Guo, Q., et al. 2011, *MNRAS*, 413, 101 (Guo11)
- Guo Q., White S., Angulo R. E., Henriques B., Lemson G., Boylan-Kolchin M., Thomas P., Short C. 2013, *MNRAS*, 428, 1351 (Guo13)
- Haan S., Schinnerer E., Emsellem E., García-Burillo S., Combes F., Mundell C. G., Rix H. W. 2009, *ApJ*, 692, 1623
- Jaffe, W. 1983, *MNRAS*, 202, 995
- Kalnajs A. J., 1972, *ApJ*, 11, 41
- Kauffmann, G. 1996, *MNRAS*, 281, 475
- Kauffmann, G., et al. 2012, *MNRAS*, 422, 997
- Kewley, L. J., Rupke, D., Zahid, H. J., Geller, M. J., & Barton, E. J. 2010, *ApJL*, 721, L48
- Keres, D., Yun, M. S., & Young, J. S. 2003, *ApJ*, 582, 659
- Komatsu, E., et al. 2011, *ApJS*, 192, 18
- Krumholz, M. R., McKee, C. F., & Tumlinson, J. 2009, *ApJ*, 693, 216
- Kuhlen, M., Krumholz, M. R., Madau, P., Smith, B. D., & Wise, J. 2012, *ApJ*, 749, 36
- Lacey, C. G., & Fall, S. M. 1985, *ApJ*, 290, 154
- Lagos, C. D. P., Lacey, C. G., Baugh, C. M., Bower, R. G., & Benson, A. J. 2011, *MNRAS*, 416, 1566
- Larson R. B., 1976, *MNRAS*, 176, 31
- Leroy, A. K., Walter, F., Brinks, E., Bigiel, F., de Blok, W. J. G., Madore, B., & Thornley, M. D. 2008, *AJ*, 136, 2782
- Leroy, A. K., et al. 2009, *AJ*, 137, 4670
- Leroy, A. K., et al. 2013, *arXiv:1301.2328*
- Li, C., & White, S. D. M. 2009, *MNRAS*, 398, 2177
- Levine, E. S., Blitz, L., & Heiles, C. 2006, *ApJ*, 643, 881
- Lo K. Y., Sargent W. L. W., Young K., 1993, *AJ*, 106, 507
- Luck R. E., Gieren W. P., Andrievsky S. M., Kovtyukh V. V., Fouqué P., Pont F., Kienzie F., 2003, *A&A*, 401, 939
- Luo Z. J., Chen J. Z., Mo H., Shu C. G., Huang J.-S., Chen Z., 2011, *ASPC*, 446, 227
- Magrini, L., Vílchez, J. M., Mampaso, A., Corradi, R. L. M., & Leisy, P. 2007, *A&A*, 470, 865
- Marigo, P. 2001, *A&A*, 370, 194
- Martin C. L., 1996, *ApJ*, 465, 680
- Martin C. L., Kobulnicky H. A., Heckman T. M., 2002, *ApJ*, 574, 663
- Martin A. M., Papastergis E., Giovanelli R., Haynes M. P., Springob C. M., Stierwalt S., 2010, *ApJ*, 723, 1359
- Matteucci F., Francois P., 1989, *MNRAS*, 239, 885
- McKee, C. F., & Krumholz, M. R. 2010, *ApJ*, 709, 308
- Mo, H. J., Mao, S., & White, S. D. M. 1998, *MNRAS*, 295, 319
- Moran, S. M., et al. 2012, *ApJ*, 745, 66 (Moran12)
- Moustakas J., Kennicutt R. C., Jr., Tremonti C. A., Dale D. A., Smith J.-D. T., Calzetti D., 2010, *ApJS*, 190, 233
- Obreschkow, D., Croton, D., DeLucia, G., Khochfar, S., & Rawlings, S. 2009, *ApJ*, 698, 1467
- Obreschkow, D., & Rawlings, S. 2009, *MNRAS*, 394, 1857
- Pettini, M., & Pagel, B. E. J. 2004, *MNRAS*, 348, L59
- Power, C., Baugh, C. M., & Lacey, C. G. 2010, *MNRAS*, 406, 43
- Portinari, L., & Chiosi, C. 2000, *A&A*, 355, 929
- Prantzos, N. 1999, *Ap&SS*, 265, 411
- Robertson B. E., Kravtsov A. V., 2008, *ApJ*, 680, 1083
- Rudolph A. L., Fich M., Bell G. R., Norsen T., Simpson J. P., Haas M. R., Erickson E. F., 2006, *ApJS*, 162, 346
- Rupke, D. S. N., Kewley, L. J., & Chien, L.-H. 2010, *ApJ*, 723, 1255
- Saintonge, A., et al. 2011, *MNRAS*, 415, 32
- Saintonge A., et al., 2011, *MNRAS*, 415, 61
- Schönrich, R., & Binney, J. 2009, *MNRAS*, 396, 203
- Schruba, A., et al. 2011, *AJ*, 142, 37
- Somerville, R. S., Primack, J. R., & Faber, S. M. 2001, *MNRAS*, 320, 504
- Spergel D. N., et al., 2003, *ApJS*, 148, 175
- Spitoni, E., & Matteucci, F. 2011, *A&A*, 531, A72
- Springel V., et al., 2005, *Natur*, 435, 629
- Stil J. M., Israel F. P., 2002, *A&A*, 389, 29
- Strickland D. K., Heckman T. M., Colbert E. J. M., Hoopes C. G., Weaver K. A., 2004, *ApJS*, 151, 193
- Tinsley B. M., Larson R. B., 1978, *ApJ*, 221, 554
- van den Bosch F. C., 1998, *ApJ*, 507, 601
- Walter, F., Brinks, E., de Blok, W. J. G., Bigiel, F., Kennicutt, R. C., Thornley, M. D., & Leroy, A. 2008, *AJ*, 136, 2563
- Weinmann S. M., Kauffmann G., von der Linden A., De Lucia G., 2010, *MNRAS*, 406, 2249
- Wong T., Blitz L., Bosma A., 2004, *ApJ*, 605, 183
- Yin J., Hou J. L., Prantzos N., Boissier S., Chang R. X., Shen S. Y., Zhang B., 2009, *A&A*, 505, 497
- Young, J. S., et al. 1995, *ApJS*, 98, 219
- Zaritsky D., Kennicutt R. C., Jr., Huchra J. P., 1994, *ApJ*, 420, 87
- Zhang, X., & Buta, R. J. 2012, *arXiv:1203.5334*
- Zwaan, M. A., Meyer, M. J., Staveley-Smith, L., & Webster, R. L. 2005, *MNRAS*, 359, L30